

First-principles study of point defects in chalcopyrite ZnSnP₂

Yu Kumagai*

Materials Research Center for Element Strategy, Tokyo Institute of Technology, Yokohama 226-8503, Japan

Minseok Choi

Advanced Characterization and Analysis Group, Korea Institute of Materials Science, Gyeongnam 642-831, Korea

Yoshitaro Nose

Department of Materials Science and Engineering, Kyoto University, Kyoto 606-8501, Japan

Fumiyasu Oba

*Department of Materials Science and Engineering, Kyoto University, Kyoto 606-8501, Japan
and Materials Research Center for Element Strategy, Tokyo Institute of Technology, Yokohama 226-8503, Japan*

(Received 15 July 2014; published 22 September 2014)

Chalcopyrite ZnSnP₂ is an alternative photoabsorber material for solar cells because of its controllable band gap, high absorption coefficient, and earth abundant constituents. In this study we systematically investigate its native point defects including vacancies, interstitials, and antisites using first-principles calculations with the Heyd-Scuseria-Ernzerhof hybrid functional. We evaluate the defect formation energies and defect single-particle levels at the dilute limit using finite-size image-charge corrections and compare them with those reported for CuInSe₂ and CuGaSe₂. The most likely donors and acceptors are cation antisites, Sn-on-Zn and Zn-on-Sn, respectively. Because of their significantly low formation energies, they lead to Fermi level pinning in the band gap under any growth condition, and constrain the carrier concentration. The Sn-on-Zn antisite in the neutral charge state becomes an intrinsic DX center, a complex of the Sn interstitial and Zn vacancy, and shows a deep donor level as reported for CuGaSe₂.

DOI: [10.1103/PhysRevB.90.125202](https://doi.org/10.1103/PhysRevB.90.125202)

PACS number(s): 61.72.J-, 61.72.Bb, 71.20.Nr

I. INTRODUCTION

CuInSe₂ (CIS), a ternary I-III-VI₂ chalcopyrite, is a photoabsorber material for highly efficient photovoltaic cells because of its high absorption coefficient [1], benign grain boundaries [2], and good thermal stability [3]. By mixing CIS (band gap, $E_g = 1.05$ eV) with CuGaSe₂ (CGS) with $E_g = 1.68$ eV, the band gap can be tuned to match the solar spectrum. Currently the efficiency of CuIn_{1-x}Ga_xSe₂ based cells can be beyond 20% [4]. It is, however, technologically more worthwhile if expensive and scarce In and Ga are replaced by inexpensive and earth abundant species.

A promising candidate for an alternative photoabsorber material is II-IV-V₂ chalcopyrite ZnSnP₂. The constituents Zn and Sn are well mined, and the direct band gap of 1.68 eV [5] is close to the optimum value at the Shockley-Quisser limit [6]. The absorption coefficient is high and almost comparable with CGS ($>10^4$ cm⁻¹ above 1.9 eV) [7]. In addition, when temperature is increased to 990 K, cation disorder occurs and consequently a sphalerite structure with a lower band gap emerges [1]. The change of the cooling rate during crystallization makes it possible to obtain crystals with various degrees of cation ordering. The experimentally reported band gaps of the sphalerite ZnSnP₂ range from 1.22 to 1.38 eV, and hence fine tuning of the band gap may be attained via the control of cation ordering [5,8,9]. The band gap can also be

tuned by alloying with CdSnP₂ [7], which is isostructural to ZnSnP₂ and has a smaller direct gap of 1.17 eV [10].

In semiconductors, native point defects can dominate the electronic properties, leading to unintentional conductivity and carrier recombination. Undoped ZnSnP₂ is known to be a *p*-type semiconductor. Rubenstein and Ure prepared ZnSnP₂ by a solution growth method under a tin excess condition, and observed *p*-type conductivity using Hall and room temperature thermoelectric probe measurements [11]. Their chemical analysis suggested that Zn is deficient compared to Sn and P in the samples and, therefore, the source of the *p*-type conductivity is possibly Zn vacancies. Miyauchi *et al.* observed a donor-acceptor transition level in ZnSnP₂ crystals grown by solution growth and normal freezing methods [12]. From the difference in the photoluminescence spectra before and after annealing under a Zn atmosphere, they speculated that Sn-on-Zn antisites and Zn vacancies act as shallow donors and acceptors, respectively.

Despite the experimental efforts, the defect physics is not well established in ZnSnP₂. In terms of technological applications, it would be important to find out whether ZnSnP₂ can be inverted to an *n*-type semiconductor by doping for the fabrication of the *p-n* homojunction solar cells. Such dopability is partly ruled by the position of the pinning level, where the formation energy of a charged defect becomes zero in the band gap [13]. When an acceptor pinning level is located near midgap, *n*-type doping is prohibited. This is because when the Fermi level is located near the CBM, acceptors associated with the pinning level have negative formation energies and spontaneously emerge until the Fermi level is decreased to the

*yuukuma@gmail.com

pinning level. Demers and van de Walle have reported that P interstitials form a deep acceptor pinning level in Zn_3P_2 , hindering its n -type doping [14]. Persson *et al.* have also shown a deep pinning level of the Cu vacancy in CGS, which has almost the same band gap as ZnSnP_2 ($E_g = 1.68$ eV) [13]. Regarding CIS and CGS, a wide variety of defects have been theoretically investigated [13,15–20]. Lany and Zunger have reported using the local density approximation (LDA) that intrinsic DX centers and a metastable state of the Se vacancy exist in CIS and CGS [16,17,21]. Recently, Pohl and Albe systematically revisited the native defects in CIS and CGS using a hybrid functional, and carefully analyzed the results in comparison with previous theoretical and experimental findings [19]. In this study we systematically investigate native defects in ZnSnP_2 using first-principles calculations and compare the defect properties to those in CIS and CGS to find whether the defect physics observed in CIS and CGS holds in II-IV- V_2 chalcopyrite ZnSnP_2 . We have adopted a hybrid density functional that can well reproduce the experimental band gap of ZnSnP_2 and is expected to reduce self-interaction errors that prevail in local and semilocal functionals. Furthermore, image-charge corrections are carefully applied to defect formation energies and defect single-particle levels to predict them at the dilute limit.

II. COMPUTATIONAL DETAILS

The calculations were performed using the projector augmented-wave (PAW) method [23] as implemented in VASP [24,25]. PAW data sets with radial cutoffs of 1.22, 1.59, and 1.01 Å for Zn, Sn, and P, respectively, were employed. Zn 3*d* and 4*s*, Sn 5*s* and 5*p*, and P 3*s* and 3*p* were described as valence electrons. For the perfect crystal, lattice constants and internal atomic positions were fully optimized until the residual stresses and forces converged to less than 0.03 GPa and 0.005 eV/Å, respectively. Defect calculations were performed using the theoretical lattice constants of the perfect crystal. The internal atomic positions were relaxed until the residual forces reduce to less than 0.02 eV/Å. Wave functions were expanded with a plane-wave basis set. Cutoff energies were set to 400 and 300 eV for the calculations of the perfect crystal and defective systems, respectively; the estimation of stress in the former requires a higher cutoff energy to reduce the spurious Pulay stress. Spin polarization was considered for all defects.

The LDA and generalized-gradient approximation (GGA) significantly underestimate the band gaps of semiconductors, which can lead to erroneous defect properties even qualitatively. Thus, we adopt the Heyd-Scuseria-Ernzerhof (HSE) hybrid functional [26–28], which describes the electronic structures of semiconductors and insulators more accurately than the LDA and GGA [28–31] and have been applied

to their point defects [14,19,32,33]. In the HSE functional, short-range exchange interactions are described by mixing nonlocal Hartree-Fock (HF) exchange into the exchange of the Perdew-Burke-Ernzerhof generalized-gradient approximation (PBE) [34]. The screening parameter and mixing of HF exchange were set at the HSE06 values of 0.208 Å^{−1} and 0.25 throughout this study [28].

The formation energy of a point defect is calculated as [35–37]

$$E_f[D^q] = \{E[D^q] + E_{\text{corr}}[D^q]\} - E_P - \sum n_i \mu_i + q(\epsilon_{\text{VBM}} + \Delta\epsilon_F), \quad (1)$$

where $E[D^q]$ and E_P are the total energies of the supercell with defect D in charge state q and the perfect crystal supercell without any defect, respectively. n_i is the number of removed ($n_i < 0$) or added ($n_i > 0$) i -type atoms and μ_i refers to the chemical potential. The chemical potentials can be controlled within the range where the host system is stable. We calculated a Zn-Sn-P chemical potential diagram at 0 K (see details in Sec. III B), and determined the region of allowed chemical potentials. ϵ_{VBM} is the energy level of the valence band maximum (VBM). $\epsilon_{\text{VBM}} + \Delta\epsilon_F$ represents the Fermi level, and $\Delta\epsilon_F$ changes within the band gap. Apart from the approximated exchange-correlation functional, an error in the defect formation energy mainly comes from the spurious electrostatic interactions between the periodically repeated cells, and $E_{\text{corr}}[D^q]$ corresponds to correction energy for it (see Sec. III C in detail). Note that the potential alignment is not considered because it is unnecessary when the image-charge correction is properly applied to the defect formation energy [37].

For defect calculations, a 64-atom supercell constructed by expanding the conventional unit cell [Fig 1(a)] and a Γ centered $2 \times 2 \times 2$ k -point sampling for the reciprocal space integration were employed based on the test calculations shown in Sec. III C. Calculations with a 216-atom supercell constructed from the primitive unit cell and a Γ -only k -point sampling were also performed to complement the 64-atom supercell calculations. Almost the same results were obtained using these two sets of calculations. In the case where different charge states of a defect give rise to different atomic configurations, we performed calculations using the structures converged at other charge states, and compared their energies after applying the finite-size correction to find out the lowest energy configuration. Such multiple configurations appeared in Sn and P vacancies, and Zn, Sn, and P interstitials. The Fermi level at which the formation energies of a defect in different charge states equalize is referred to as thermodynamical transition level. From Eq. (1), the thermodynamical transition level between charge states q and q' $\epsilon^{\text{TTL}}(D, q/q')$ is written with respect to the VBM as

$$\epsilon^{\text{TTL}}(D, q/q') = -\frac{\{E[D^q] + E_{\text{corr}}[D^q]\} - \{E[D^{q'}] + E_{\text{corr}}[D^{q'}]\}}{q - q'} - \epsilon_{\text{VBM}}. \quad (2)$$

Its position with respect to the conduction band minimum (CBM) or VBM corresponds to the thermal ionization energy of a donor or acceptor.

III. RESULTS AND DISCUSSION

A. Fundamental properties of perfect crystals

The Bravais lattice of the chalcopyrite structure is the body-centered tetragonal. There are eight atoms in the primitive unit cell [Fig. 1(a)], and its space group is $I\bar{4}2m$. Each anion (cation) is surrounded by four nearest neighbor cations (anions) as in the zincblende structure. In ZnSnP_2 , Zn and Sn are coordinated by four P, while P is coordinated by two Zn and two Sn. Table I summarizes band gaps, lattice constants, and displacement parameters of P calculated using the LDA as parametrized by Perdew and Zunger [38], PBE [34], PBE+ U [39] ($U - J = U_{\text{eff}} = 7$ eV), which corrects on-site

TABLE I. Band gap E_g , lattice constants a and c , their ratio, and displacement parameter u of P in ZnSnP_2 calculated using different exchange-correlation functionals. The band gap of mBJ is estimated with the relaxed structure by HSE06. Note that both VBM and CBM are located at the Γ point in any result. For PBE+ U , the effective on-site Coulomb potential of $U - J = U_{\text{eff}}$ at Zn-3d orbitals was set at a typical value of 7 eV.

	E_g (eV)	a (Å)	c (Å)	c/a	u
LDA	0.83	5.58	11.20	2.01	0.22
PBE	0.69	5.71	11.44	2.01	0.23
PBE+ U	0.89	5.69	11.41	2.01	0.23
TPSS	0.92	5.67	11.35	2.00	0.23
rTPSS	1.01	5.64	11.27	2.00	0.23
HSE06	1.68	5.67	11.36	2.00	0.23
mBJ	1.71	—	—	—	—
Expt. [5,22]	1.68	5.651	11.302	2.00	0.24

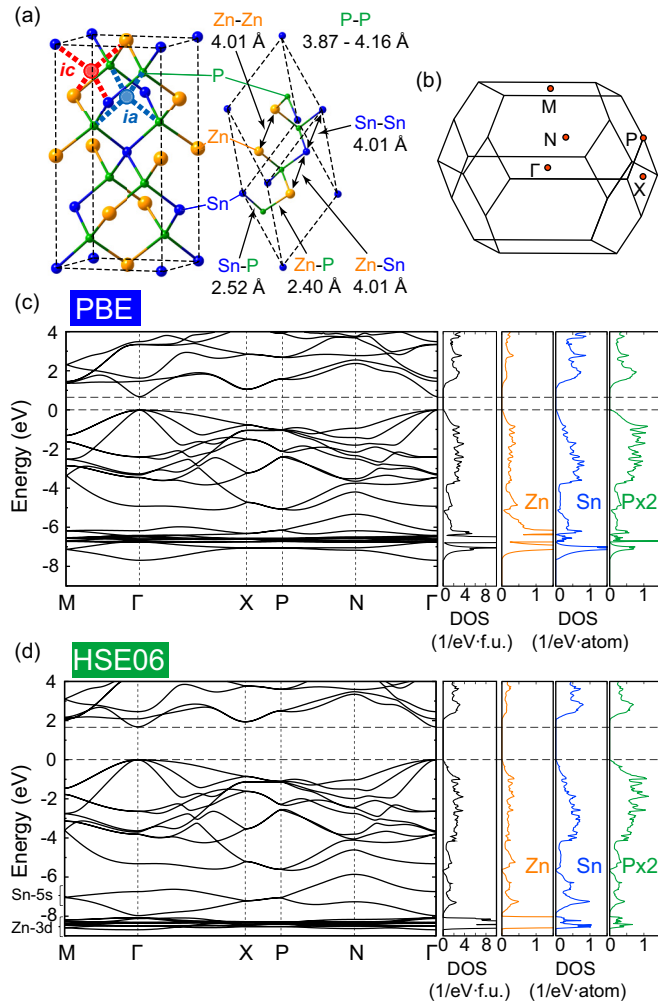


FIG. 1. (Color online) (a) Conventional and primitive unit cells of chalcopyrite ZnSnP_2 . Interstitial sites surrounded by four cations and four anions, respectively, represented as ic and ia and interatomic distances are also shown. Note that the P-P distances of the second nearest neighbors are widespread because of the displacements of P from the corresponding positions in the zincblende structure. (b) Brillouin zone of ZnSnP_2 in the body-centered tetragonal system and its high symmetry points. (c) and (d) Calculated band structure and density of states for ZnSnP_2 using (c) PBE and (d) HSE06. The energy zeros are set at the VBM. Horizontal dashed lines indicate the VBM and CBM. Note that the density of states near the CBM is significantly small due to a large band dispersion.

Coulomb interactions in the selected localized orbitals (Zn-3d in the present case) and improves their electronic structures [40–42], Tao-Perdew-Staroverov-Scuseria (TPSS) meta-GGA [43], revised TPSS (rTPSS) [44], and HSE06 alongside experimental values. The results show typical tendencies; the band gaps calculated using the LDA, PBE, PBE+ U , TPSS, and rTPSS are significantly underestimated. The lattice constants using the LDA are underestimated while those using the GGA and GGA+ U are overestimated. The meta-GGA functionals predict lattice constants better. The band gap calculated using HSE06 shows excellent agreement with the experimental gap. This is in contrast with CIS and CGS for which we need to change the screening parameter or mixing of HF exchange in HSE functional to reproduce the experimental band gaps [18–20,31,45,46]. The lattice constants and displacement parameter are also close to the experimental values. We also calculated the band gap using modified Becke-Johnson (mBJ) potential [47] at the HSE06 theoretical lattice constants. It also excellently agrees with the experimental gap.

The band structure and density of states (DOS) obtained using PBE and HSE06 are shown in Figs. 1(c) and 1(d). The total DOS was calculated using the tetrahedron method with Blöchl corrections [48]. The projected density of states (PDOS) was evaluated within the spheres centered on the atomic sites with radii of 1.27, 1.57, and 1.23 Å for Zn, Sn, and P, respectively. Between the PBE and HSE06 calculations, the shapes of the valence and conduction bands are almost the same, respectively. Both reproduce the direct-type band structure, although the band gaps are different. Due to a larger self-interaction error in PBE, the position of the Zn-3d band using PBE is 2 eV higher than that using HSE06, and the position changes with respect to the Sn-5s band. The VBM at the Γ point is mainly composed of P orbitals with slight hybridization with Zn and Sn orbitals. The antibonding characteristics between cation and anion orbitals at the valence band are not so pronounced in ZnSnP_2 compared with CIS and CGS, since the Zn-3d states are much deeper than the Cu-3d states. On the other hand, the CBM, which also locates at the Γ point, is primarily composed of Zn and Sn orbitals.

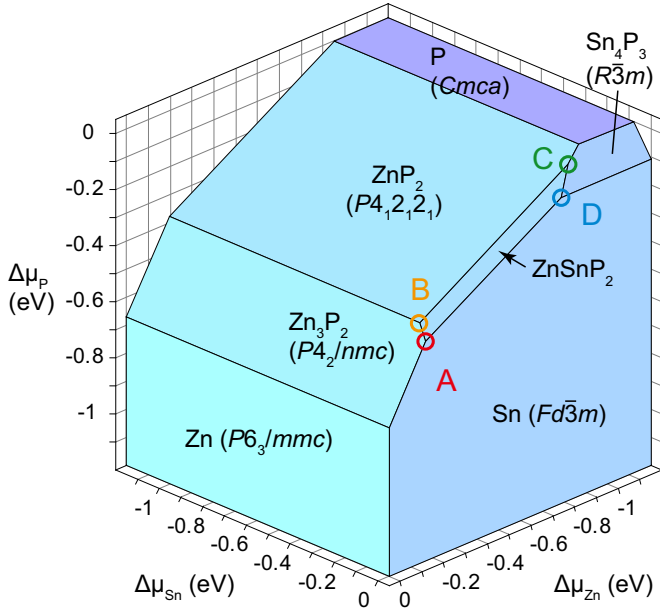


FIG. 2. (Color online) Chemical potential diagram for the Zn-Sn-P ternary system involving ZnSnP_2 and its competing phases obtained using HSE06. The space groups of the most stable structures are shown in brackets. The four vertices of the ZnSnP_2 stable region are labeled A–D and the corresponding chemical potentials are listed in Table II. The chemical potential of element i $\Delta\mu_i$ is defined with respect to that of element i in its standard state μ_i° as $\Delta\mu_i = \mu_i - \mu_i^\circ$. The standard states of Zn, Sn, and P are set to the solid $\text{Zn}(\text{P}6_3/\text{mmc})$, $\text{Sn}(\text{Fd}\bar{3}\text{m})$, and $\text{P}(\text{Cmca})$. The calculated heats of formation of Zn_3P_2 , ZnP_2 , Sn_4P_3 , and ZnSnP_2 are -1.35 , -0.95 , -0.33 , and -1.01 eV/formula unit, respectively.

B. Chemical potential diagram

As shown in Eq. (1), defect formation energies depend on the chemical potentials. Under an equilibrium condition, the chemical potentials are constrained by the formation of competing phases. Here the region of the chemical potentials is determined using HSE06 total energies. We considered $\text{Zn}(\text{P}6_3/\text{mmc})$, $\text{Sn}(\text{Fd}\bar{3}\text{m}$ and $I4_1/\text{amd})$, $\text{P}(\text{Cmca})$, $\text{Zn}_3\text{P}_2(\text{P}4_2/\text{nmc})$, $\text{ZnP}_2(\text{P}2_1/\text{c}$ and $\text{P}4_12_12)$, and $\text{Sn}_4\text{P}_3(\text{R}\bar{3}\text{m})$ as competing phases. We found that the $\text{Fd}\bar{3}\text{m}$ and $\text{P}2_1/\text{c}$ structures are stable for Sn and ZnP_2 , respectively. The entropy contributions are neglected since they are expected to be small for these solid phases and partly cancel out.

Figure 2 shows the calculated chemical potential diagram for the Zn-Sn-P ternary system. The values at the four vertices of the stable region of ZnSnP_2 are labeled A–D and listed in Table II. The range of the chemical potentials directly

TABLE II. Chemical potentials of the constituent atoms of ZnSnP_2 at points A–D in Fig. 2 ($\Delta\mu_i$ in eV).

Point	$\Delta\mu_{\text{Zn}}$	$\Delta\mu_{\text{Sn}}$	$\Delta\mu_{\text{P}}$
A	-0.17	0	-0.42
B	-0.20	-0.05	-0.38
C	-0.88	-0.05	-0.04
D	-0.79	0	-0.11

affects the controllability of defect concentrations via growth conditions. It is noteworthy that the allowed chemical potential of Zn ranges between -0.88 and -0.17 eV, whereas that of Sn between -0.05 and 0 eV, meaning the control of the Sn chemical potential is difficult by changing growth conditions. This would be in part due to the difference of the cohesive energies between the Zn and Sn metals. The calculated (experimental [49]) cohesive energies of Zn and Sn are 1.17 (1.35) and 3.13 (3.14) eV, respectively, which indicates that the Sn metal is much more stable, and consequently the stable region of ZnSnP_2 is largely reduced.

C. Corrections on defect formation energies and defect single particle levels

When performing charged defect calculations, we should address finite-size image-charge corrections on defect formation energies. In this study such corrections were performed with the scheme proposed by Freysoldt, Neugebauer, and Van de Walle (FNV) [50] with our extensions described in Ref. [37]. Starting from the point charge (PC) model, the correction energy of the FNV scheme is written as

$$E_{\text{FNV}} = E_{\text{PC}} - q \Delta V_{\text{PC},q/b}|_{\text{far}}, \quad (3)$$

where E_{PC} is the screened Madelung energy. $\Delta V_{\text{PC},q/b}$ denotes the difference between the defect-induced potential with respect to the bulk potential and the PC potential, and $\Delta V_{\text{PC},q/b}|_{\text{far}}$ is $\Delta V_{\text{PC},q/b}$ at a place far from the defect in the supercell [37,50–53]. Our implementation uses atomic site electrostatic potential for determining the defect-induced potential, which has been shown to be effective for relaxed atomic configurations [37]. The atomic site potential was evaluated in the spheres with radii of 0.95 , 1.41 , and 0.96 Å for Zn, Sn, and P, respectively. We have tested this scheme with sets of calculations using various supercell sizes for the Sn vacancy with $q = -4$ (V_{Sn}^{-4}) and Zn-on-Sn antisite with $q = -2$ ($\text{Zn}_{\text{Sn}}^{-2}$), both of which do not involve perturbed host states (PHS) with electron and hole occupation for donorlike and acceptorlike states, respectively. Test calculations were performed using PBE since HSE06 calculations using large supercells are computationally too expensive.

Our extension of the FNV correction scheme uses a static dielectric tensor, namely the sum of the ion-clamped dielectric tensor (ϵ^{ele}) and ionic contribution (ϵ^{ion}), to account for anisotropic screening [37]. For the PBE test calculations we obtained them using density functional perturbation theory with PBE [54,55]. The electronic part includes local field effects. In tetragonal systems, only diagonal components are nonzeros and ϵ_{11} and ϵ_{33} are independent. The calculated $\epsilon_{11}^{\text{ele}}$, $\epsilon_{33}^{\text{ele}}$, $\epsilon_{11}^{\text{ion}}$, and $\epsilon_{33}^{\text{ion}}$ are 11.69 , 11.96 , 2.36 , and 2.55 , respectively. We can see that ϵ^{ele} mainly contribute to the static dielectric tensor rather than ϵ^{ion} , and anisotropy is rather small in ZnSnP_2 . The latter would be related to the fact that the chalcopyrite structure is close to the cubic zincblende structure. In the HSE06 defect calculations we used the summation of the electronic part calculated using HSE06 and the ionic part calculated using PBE+ U , the latter of which would be acceptable because the ionic contributions are much smaller than the electronic components. The calculated $\epsilon_{11}^{\text{ele}}$ and $\epsilon_{33}^{\text{ele}}$ using HSE06 with a finite electric field approach are

9.49 and 9.58. These are smaller than the PBE values partly due to the increase of the band gap by HSE06. The ionic contributions of PBE+ U are $\epsilon_{11}^{\text{le}} = 2.51$ and $\epsilon_{33}^{\text{le}} = 2.88$.

Figures 3(a) and 3(b) show the formation energies of V_{Sn}^{-4} and Zn_{Sn}^{-2} using various supercells constructed by expanding the conventional and primitive unit cells. Without any correction, significant cell size dependencies exist; an error in $E_f[V_{\text{Sn}}^{-4}]$ amounts to 2.4 eV with the 64-atom supercell. Using the extended FNV scheme, $E_f[V_{\text{Sn}}^{-4}]$ and $E_f[Zn_{\text{Sn}}^{-2}]$ are well corrected, and the cell size dependencies are drastically reduced. As shown in Figs. 3(a) and 3(b), after the corrections, calculations with the 64-atom supercell and a Γ -centered $2 \times 2 \times 2$ k -point sampling are slightly more accurate than those with the 216-atom supercell and a Γ -only k -point sampling.

The electrostatics-based correction energy up to the L^{-3} order, where L is the dimension of a supercell, is null for

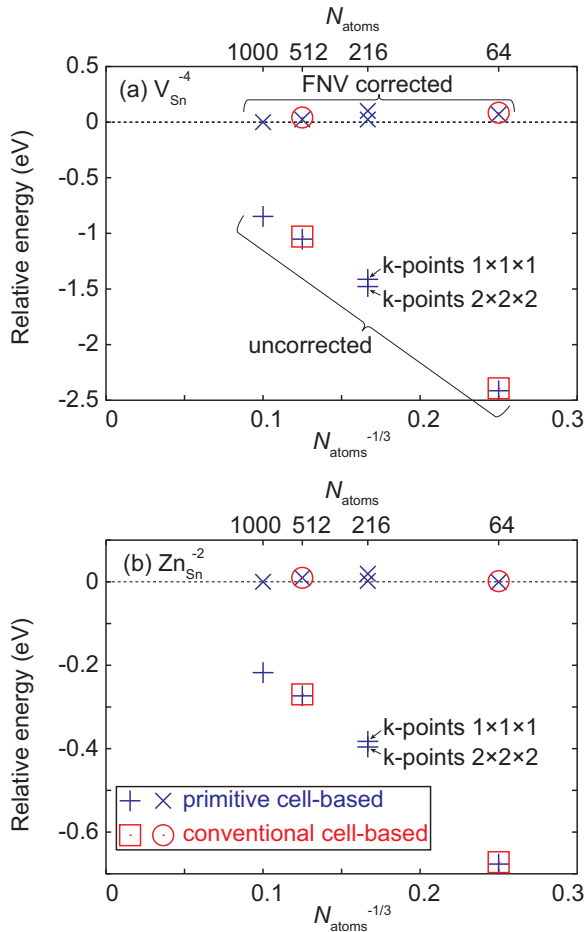


FIG. 3. (Color online) Uncorrected and FNV corrected relative formation energies of (a) V_{Sn}^{-4} and (b) Zn_{Sn}^{-2} as a function of the supercell size and shape. N_{atom} is the number of atoms in the supercell before introducing a defect. The 64- and 216-atom supercells were used with a Γ -centered $2 \times 2 \times 2$ k -point sampling, and 512- and 1000-atom supercells were with a Γ -only k -point sampling. The 216-atom supercell with a Γ -only k -point sampling was also considered. Calculations were performed using PBE. Zeros of the relative energies are set to the corrected energies calculated with 1000-atom supercells.

neutral defects [57]. This is, however, true only for the cases where defect-induced charges are localized within supercells. As shown in Fig. 4(a), the formation energy of neutral Zn_{Sn}^0 has a cell size dependence similar to that of Zn_{Sn}^{-2} . This is because two holes occupy delocalized acceptorlike states and spill out from the supercells. The charge of the acceptorlike states significantly overlaps with their images and acts like the background charge [58]. The same behavior has been reported for the neutral Zn interstitial in ZnO [58] and some neutral defects in InP [59]. In general, this can be expected for not only neutral but also charged defects with PHS. Without a correction, the error in $E_f[Zn_{\text{Sn}}^0]$ is estimated to be roughly 0.5 eV with the 64-atom supercell; thus we need a special treatment for such defects. When calculating the native defects in ZnO using hybrid functionals, Oba *et al.* estimated the correction energies of defects with PHS by extrapolating the defect formation energies obtained with a set of different supercell size and shape using the GGA [58]. This procedure cannot account for the difference between defect

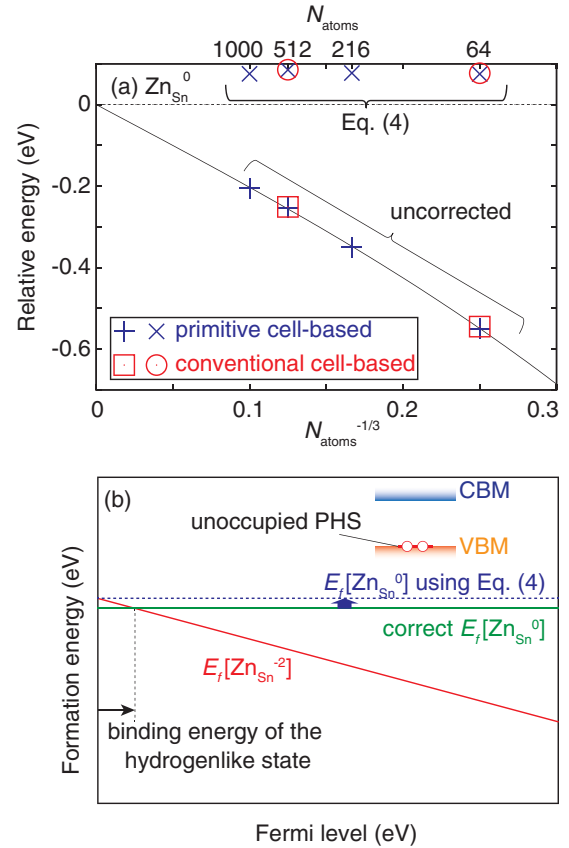


FIG. 4. (Color online) (a) Uncorrected Zn_{Sn}^0 formation energies and those obtained by Eq. (4). The supercell and k -point sampling sets are the same as those in Fig. 3, and the band dispersion corrections for shallow acceptor states [56] are applied for the 64- and 216-atom supercells with $2 \times 2 \times 2$ sampling. Zero of the relative energy is set to the extrapolated value using a function of $aN_{\text{atoms}}^{-1} + bN_{\text{atoms}}^{-1/3} + c$. It is noteworthy that the energy of neutral Zn_{Sn}^0 shows a significant cell size dependence, but it is reduced to less than 0.1 eV when using Eq. (4). (b) Schematic of the approximation using Eq. (4). Since the binding energy of the hydrogenlike state is approximated to be zero, the energy of the defect with PHS is overestimated in any case.

states calculated using the GGA and HSE06. We may instead directly calculate defects with PHS using a gigantic supercell, but it is unrealistic using HSE06. For instance, a 64 000-atom supercell is indispensable for an accurate estimation of shallow acceptor levels in Si [60].

Here we use an alternative way to estimate the energies of defects with PHS. The thermal ionization energy of the defect with PHS basically corresponds to its hydrogenlike binding energy, and is typically less than 0.1 eV. When its ionization energy is approximated to be zero, the energy of a defect with unoccupied acceptorlike (occupied donorlike) PHS becomes the same as the case where the PHS is occupied (unoccupied) with the Fermi level at the VBM (CBM). A schematic explanation is illustrated in Fig. 4(b). Then, the energy of the defect with unoccupied acceptorlike PHS can be written as

$$E_f[D^q] = E_f[D^{q'}]|_{\Delta\epsilon_F=0} + q\Delta\epsilon_F, \quad (4)$$

and that of the defect with occupied donorlike PHS as

$$E_f[D^q] = E_f[D^{q'}]|_{\Delta\epsilon_F=E_g} + q(\Delta\epsilon_F - E_g), \quad (5)$$

where $E_f[D^{q'}]$ is the energy of the defect without unoccupied acceptorlike or occupied donorlike PHS in charge state q' and, therefore, $q - q'$ is the charge of PHS, which is positive for acceptorlike states and negative for donorlike states. As shown in Fig. 4(a), this approximation significantly reduces the cell-size dependence to less than 0.1 eV.

It is also known that defect single-particle levels have cell size dependencies and the corrections also need to be accounted for [52,61–63]. In this study we performed the corrections based on the scheme proposed by Komsa *et al.* [52] and Chen and Pasquarello [63]. A correction for the defect single-particle level $\Delta\epsilon^{\text{SP}}$ is related to the total-energy correction as

$$\Delta\epsilon^{\text{SP}} = -\frac{2}{q}E_{\text{corr}}, \quad (6)$$

where E_{corr} is the PC or FNV correction energy. Komsa *et al.* extrapolated the vacancy levels in diamond to the infinite interdefect distance limit using the point-charge correction energies [52]. Chen and Pasquarello used the FNV correction energies to estimate the F^+ center single-particle level in LiF [63]. We tested performances of these two schemes for the P interstitial surrounded by anions in the +1 charge state (P_{ia}^{+1}) and the Sn vacancy in the -4 charge state (V_{Sn}^{-4}). The defect single-particle levels are determined by taking the Brillouin-zone average [36]. As shown in Fig. 5, the FNV corrections overshoot their single-particle levels, whereas the PC corrections perform better. When deriving Eq. (6), the short-range Coulomb interaction is assumed to be screened by a scalar dielectric constant, but this might not be appropriate for defect single-particle level corrections [63]. Based on the test results shown in Fig. 5, we adopt Eq. (6) with the PC correction energies.

D. Native point defects

In the present study we have studied 11 types of native point defects: Zn, Sn, and P vacancies (V_X , $X = \text{Zn, Sn, and P}$), Zn, Sn, and P interstitials at the *ic* and *ia* sites

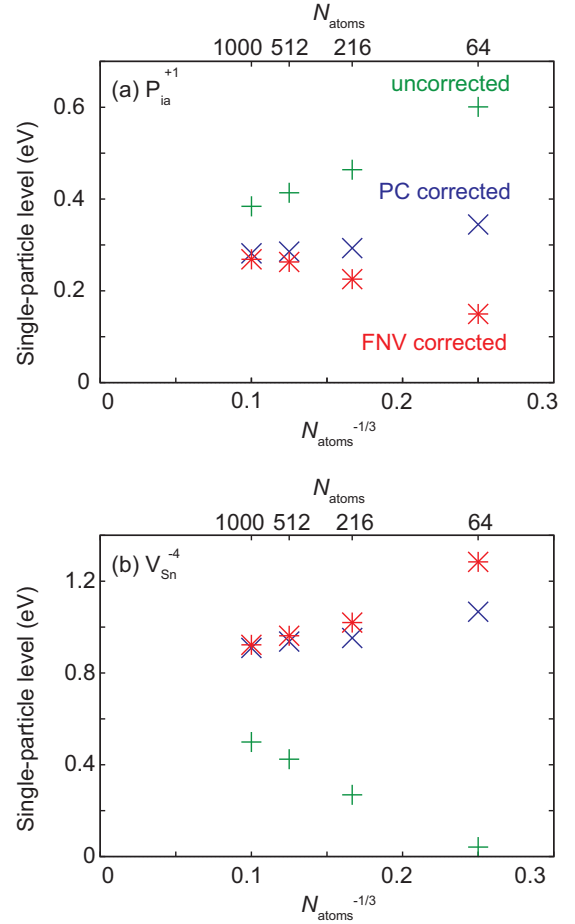


FIG. 5. (Color online) Uncorrected and corrected defect single-particle levels by adding $-\frac{2}{q}E_{\text{corr}}$ of (a) P_{ia}^{+1} [for the lower occupied in-gap state shown in Fig. 7(s)] and (b) V_{Sn}^{-4} [for the upper occupied in-gap state shown in Fig. 6(g)] with respect to the VBM as a function of the supercell size. PC and FNV corrections were used for E_{corr} (see text in detail). The VBM was obtained from the calculation of the perfect crystal. The supercells were constructed by expanding the primitive cell, and PBE was adopted. All calculations were performed with a Γ -centered $2 \times 2 \times 2$ k -point sampling to enhance the accuracy. Note that the defect single-particle levels of V_{Sn}^{-4} are located in the band gap when using PBE, but it is below the VBM when using HSE06 and the 64-atom supercell before the cell-size correction as shown in Fig. 6(g).

(X_{ia} and X_{ic} , $X = \text{Zn, Sn, and Se}$) depicted in Fig. 1(a), and Zn-on-Sn and Sn-on-Zn cation antisites (Zn_{Sn} and Sn_{Zn}). For V_{Zn} , V_{Sn} , Zn_i , Sn_i , Zn_{Sn} , and Sn_{Zn} , we considered relevant charge states based on their formal charges. For example, the charge states of Zn_i considered are 0, +1, and +2 for the formal charge of Zn ion is +2 in ZnSnP_2 . On the other hand, it has been reported that the Se vacancy and Se interstitial in CIS and CGS are amphoteric and take both positive and negative charges depending on the Fermi level [16,17]. Thus we calculated V_P and P_i with 0, ± 1 , ± 2 , and ± 3 charges. When a defect single-particle level disperses across a bulk band edge, we adopted a discrete defect occupation scheme proposed by Schultz [64]. In the cases where defects have in-gap states, likely magnetic configurations were considered,

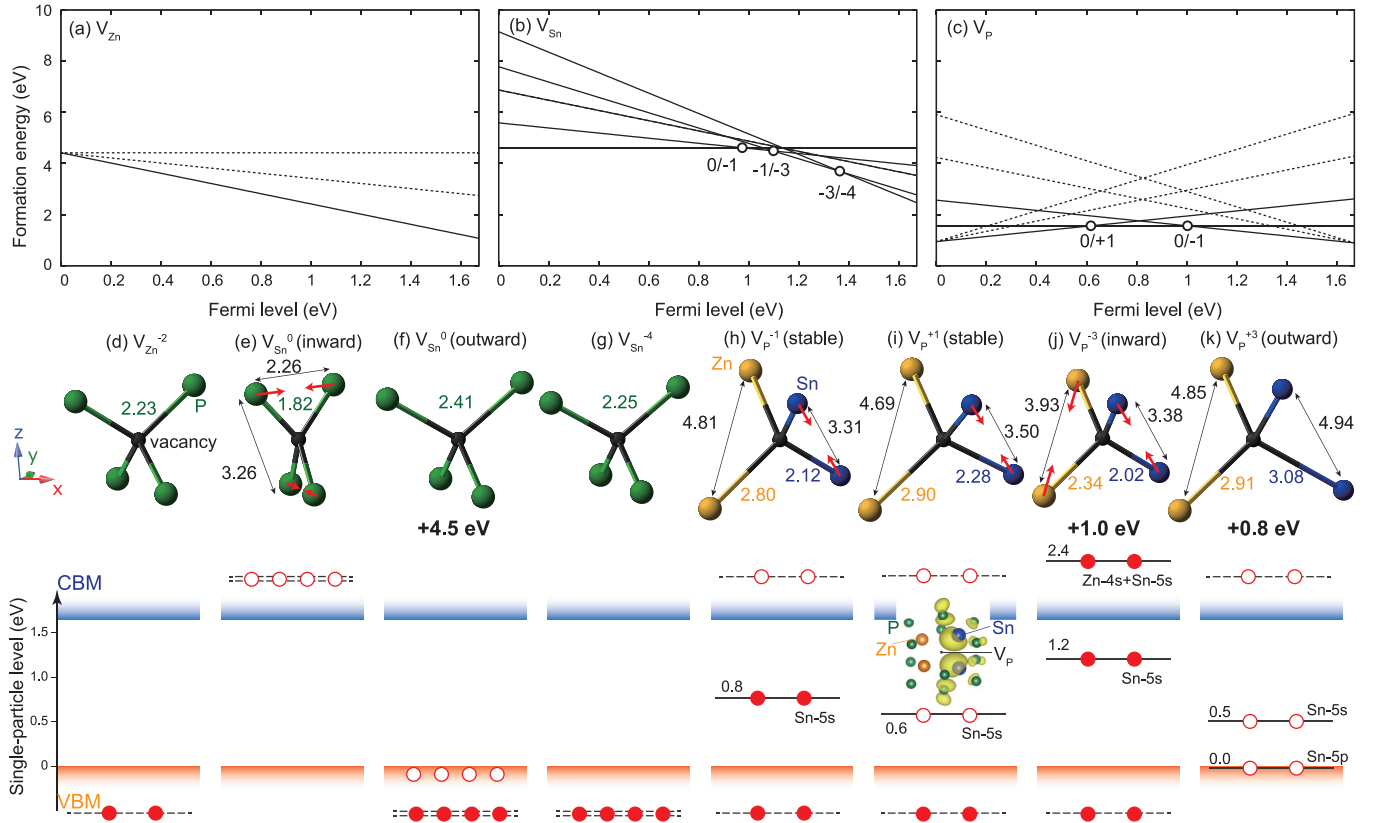


FIG. 6. (Color online) Formation energies of (a) Zn, (b) Sn, and (c) P vacancies in $ZnSnP_2$ under the Zn- and Sn-rich condition (vertex A in the chemical potential diagram in Fig. 2) as a function of the Fermi level relative to the valence band maximum (VBM), which ranges up to the conduction band minimum (CBM). For each charge state, only the energy for the most stable magnetic and atomic configuration is shown. Note that the energy of a defect with unoccupied acceptorlike (occupied donorlike) perturbed host states (PHS) is assumed to be the same at the VBM (CBM) as the case where the PHS are occupied (unoccupied) and is shown with a dashed line (see Sec. III C in detail). The positions of thermodynamical transition levels are depicted with open circles. (d)–(k) Local structures and defect single-particle levels of selected vacancies. Distances between the idealized vacancy position, which is assumed to be at the high-symmetric site, and the neighboring defects are shown in unit of Å. In any case, the VBM was obtained from the HSE06 calculation of the perfect crystal. When a defect is metastable, the energy difference from that of the most stable state is shown below the structures. In (i), the isosurface of the squared wave function for the defect state is also shown. When the defect single-particle levels are located in the valence or conduction band before the finite-size correction, they are schematically shown with dashed lines since their single-particle levels are not clearly defined. The positions of the defect single-particle levels from the VBM after the finite-size correction are shown in unit of eV. Note that in (j) an occupied defect single-particle level is located above the CBM after the correction, indicating it is an unstable state.

and only the results of the lowest energy states are shown hereafter. For instance, V_{Sn}^0 was calculated with three spin states of 0, 2, and 4 μ_B . Finally, we found that the in-gap state energetically favors low-spin states, i.e., the magnetic moment of 0 or 1 μ_B for any defect. Among the native defects considered, the candidates of donors are V_P , Zn_i , Sn_i , P_i , and Sn_{Zn} , whereas those of acceptors are V_{Zn} , V_{Sn} , V_P , P_i , and Zn_{Sn} . Figures 6, 7, and 8 show the formation energies of vacancies, interstitials, and antisites under the Zn-rich and Sn-rich condition corresponding to vertex A in Fig. 2, and local atomistic and electronic structures of selected defects. Figure 9 summarizes the thermodynamical transition levels of these defects. Defect properties are discussed in detail and compared to those reported for CIS and CGS below.

1. Vacancies

Vacancies are fundamental and important defects in many materials. In CIS (CGS), both Cu vacancy (V_{Cu}) and In (Ga)

vacancy are shallow acceptors and the Se vacancy (V_{Se}) is amphoteric and shows deep donor and acceptor transition levels [13,15–17,19,20]. Among them, only V_{Cu} has a low formation energy and is likely to affect the electrical property [15,17,19,20]. As shown in Figs. 6(a) and 6(b), V_{Zn} and V_{Sn} act as shallow and deep acceptors, respectively, in $ZnSnP_2$. V_{Zn}^{-2} has no in-gap states apart from the PHS [Fig. 6(d)], and its atomic neighbors are symmetric with inward movements of P up to 0.17 Å. V_{Zn} can be abundant when the Fermi level is located near the CBM under Zn-poor conditions. V_{Sn}^0 can be relaxed into two configurations: Neighboring P relax inwardly and outwardly as shown in Figs. 6(e) and 6(f), in which the distances between an idealized Sn vacancy position and its neighboring P are 1.81 and 2.41 Å, respectively, whereas that in perfect crystal is 2.52 Å. The inward structure is 4.5 eV lower in energy. The electronic structures are also in stark contrast with each other. The inward relaxation is nonsymmetric and forms two neighboring P-P dimer antibondings and their unoccupied defect states are pushed up above the CBM. On the other hand,

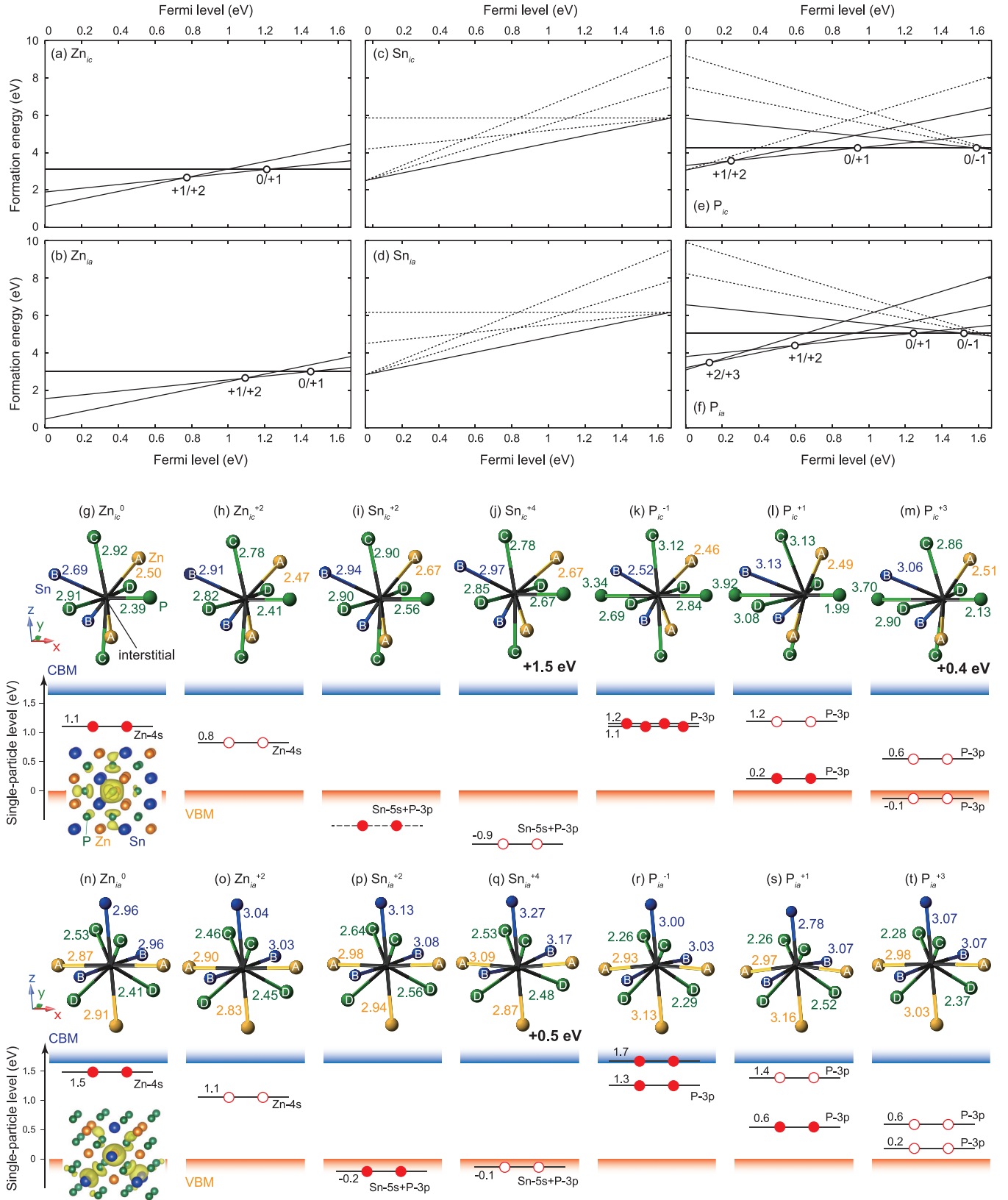


FIG. 7. (Color online) The same as Fig. 6 but for (a) and (b) Zn, (c) and (d) Sn, and (e) and (f) P interstitials at the *ic* and *ia* sites. (g)–(t) Local structures and defect single-particle levels of selected interstitials. Symmetrically equivalent atoms are labeled with alphabet symbols.

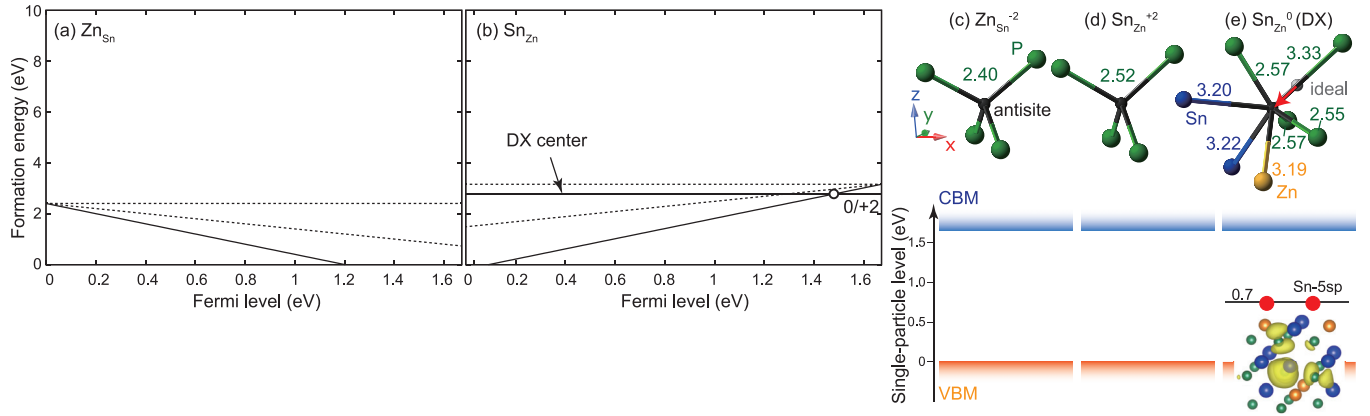


FIG. 8. (Color online) The same as Fig. 6 but for (a) Zn_{Sn} and (b) Sn_{Zn} antisites. (c)–(e) Local structures and defect single-particle levels of (c) $\text{Zn}_{\text{Sn}}^{-2}$, (d) $\text{Sn}_{\text{Zn}}^{+2}$, and (e) Sn_{Zn}^0 DX center.

the outward configuration has weak P-P bonds, leading to deep defect single-particle levels inside the valence band, and as a result four delocalized holes are placed at the VBM. Thus we can effectively write as $V_{\text{Sn}}^0(\text{outward}) \approx V_{\text{Sn}}^{-4}(\text{outward}) + 4h^+$, where h^+ indicates a hole at the VBM or acceptorlike PHS. Since an additional electron is placed at the CBM and VBM in inward and outward configurations, respectively, the difference of the energy cost to add an electron roughly corresponds to the band gap; thus the highly negatively charged V_{Sn} such as V_{Sn}^{-4} favor outward structures. V_{Sn} , however, shows a rather high formation energy and would occur in a low concentration in ZnSnP_2 .

On the other hand, V_{P} is amphoteric and show both deep donor and acceptor transition levels [Fig. 6(e)], which is similar to V_{Se} in CIS and CGS [16,17]. The situation is, however, qualitatively different in ZnSnP_2 . In the V_{P}^0 configuration, surrounding two Zn move outwardly but two Sn move inwardly and construct a singly occupied in-gap state mainly composed of an antibonding of a Sn-Sn dimer with a hybridization with P-3p [Fig. 6(i)]. V_{P}^{-1} and V_{P}^{+1} then have an occupied and an unoccupied in-gap state as shown in Figs. 6(h) and 6(i). These V_{P}^{+1} , V_{P}^0 , and V_{P}^{-1} have almost the same structure and we call this stable structure. V_{P}^{+2} has a hole at the VBM and, therefore, can be written as $V_{\text{P}}^{+2} \approx V_{\text{P}}^{+1}(\text{stable}) + h^+$, whereas V_{P}^{-2} has an electron at the CBM and so $V_{\text{P}}^{-2} \approx V_{\text{P}}^{-1}(\text{stable}) + e^-$, where e^- indicates an electron at the CBM or donorlike PHS. V_{P}^{-3} relaxes not only to $V_{\text{P}}^{-1}(\text{stable}) + 2e^-$ but to a metastable state without occupied PHS as shown in Fig. 6(j). In the latter

configuration, the neighboring two Zn are close to each other in addition to the Sn dimer and construct a bond composed mainly of Zn-4s and Sn-5s orbitals. However, the occupied defect single-particle level moves inside the conduction band after the correction, indicating this electronic structure is unstable at the dilute limit. Indeed, its formation energy is 1.0 eV higher than that of $V_{\text{P}}^{-1} + 2e^-$. V_{Se}^{+2} in CIS and CGS is also known to have a metastable configuration [17], which is similar to V_{P}^{+3} shown in Fig. 6(k). The Sn-Sn dimer bond is absent in the outward configuration, and the Sn-5p state exists in the band gap. The energy of this configuration is, however, 0.8 eV higher than that of $V_{\text{P}}^{+1}(\text{stable}) + 2h^+$. This is in contrast with the case of V_{Se} in CIS and CGS. As discussed in Ref. [16], negative- U behavior, which indicates a net attractive electron-electron interaction, can emerge as a consequence of large variation of the atomic relaxation by changing the defect charge, but it does not happen in V_{P} of ZnSnP_2 . Although V_{P} is expected to be inert for the carrier generation, it is likely to exist in a high concentration because of its low formation energy at any Fermi level.

2. Interstitials

We now discuss interstitials in ZnSnP_2 . In CIS (CGS), both Cu and In (Ga) interstitials act as shallow donors, and the Se interstitial shows deep donor and acceptor levels [18,19]. Especially the Cu interstitial has a significantly low energy and can exist in a high concentration, depending on the growth condition. Generally speaking, the stability of interstitials is ruled by the size of the space, electrostatic potential, and chemical bonding at the interstitial sites.

As shown in Figs. 7(a) and 7(b), both Zn_{ic} and Zn_{ia} show deep donor levels. The in-gap states are mainly composed of Zn-4s and P-3p orbitals [Figs. 7(g) and 7(n)]. $\text{Zn}_{\text{ia}}^{+2}$ is lower in formation energy than $\text{Zn}_{\text{ic}}^{+2}$ by 0.65 eV, whereas Zn_{ia}^0 is just 0.10 eV lower than Zn_{ic}^0 . This would be because surrounding anions lower the electrostatic potential at the *ia* site for positively charged $\text{Zn}_{\text{ia}}^{+2}$. This is also consistent with the defect single-particle levels shown in Figs. 7(g)–7(t): The defect single-particle levels are higher at the *ia* site than at the *ic* site in any defect. $\text{Zn}_{\text{ia}}^{+2}$ has a low energy when the Fermi level is located near the VBM under the Zn-rich condition. Sn_{ic} and Sn_{ia} show shallow donor behaviors, but their stable

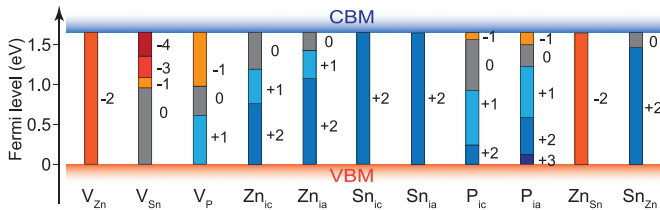


FIG. 9. (Color online) Thermodynamical transition levels of the defects considered. Among them, V_{Zn} and Zn_{Sn} are shallow acceptors, whereas Sn_{ia} and Sn_{ic} are shallow donors: The acceptor and donor levels associated with PHS are not shown in the figure.

charge states are not +4 but +2 [Figs. 7(c) and 7(d)]. Sn_{ic}^{+2} and Sn_{ia}^{+2} do not have any in-gap state, and occupied defect states composed of Sn-5s and P-3p orbitals are located below the VBM [Figs. 7(i) and 7(p)]. This indicates that the formal charge of Sn at the interstitial sites is +2. Sn_i^{+4} with unoccupied in-gap states can also be obtained but, after finite size corrections, they are found to be unstable [Figs. 7(j) and 7(q)]. Sn_{ic}^{+2} is 0.33 eV lower in formation energy than Sn_{ia}^{+2} , perhaps due to a large Sn^{+2} ionic radius. As shown in Figs. 7(e) and 7(f), P_{ic} and P_{ia} can show various charge states depending on the Fermi level and create two in-gap states comprising mainly P-3p states at both *ic* and *ia* sites except for unstable P_{ic}^{+3} . Both Sn and P interstitials have high energies at any Fermi level and cannot exist in high concentrations.

3. Antisites

Cation antisites can exist in I-III-VI₂ and II-IV-V₂ chalcopyrites. In CIS and CGS, Cu-on-In and Cu-on-Ga antisites are deep acceptors [19]. On the other hand, In-on-Cu and Ga-on-Cu antisites are shallow and deep donors [19]. They are considered to play important roles for the electrical conductivity in $\text{CuIn}_{1-x}\text{Ga}_x\text{Se}_2$ because of low formation energies of charged antisites. As shown in Figs. 8(c) and 8(d), Zn_{Sn} and Sn_{Zn} in ZnSnP_2 have no in-gap states apart from the PHS and the DX center. This is in stark contrast to CGS with almost the same band gap and band edge positions with ZnSnP_2 [65]. Zn_{Sn} and Sn_{Zn} have significantly low formation energies and would therefore be abundant under any growth condition in ZnSnP_2 . The distances of $\text{Zn}_{\text{Sn}}^{+2}$ -P and $\text{Sn}_{\text{Zn}}^{+2}$ -P are almost the same as those in Zn-P and Sn-P in the perfect crystal (see Fig. 1) and the local structures are symmetric.

In CGS, Ga_{Cu}^0 is known to be an intrinsic DX center, which traps electrons, whereas it is metastable in CIS [19]. We also calculated such a DX center in ZnSnP_2 . The atomic relaxation was started after displacing Sn from the Zn site up to 2.5 Å along the [112] direction towards the *ic* interstitial site so as to construct a complex of Sn_i and V_{Zn} [19]. Through the atomic relaxation, Sn did not return to the Zn site but remained near the interstitial site surrounded by three P. The displacement from the ideal Zn site is 1.12 Å. The defect state induced by the DX center is composed of a hybridization between Sn-5s and surrounding P-3p states. As reported in Ref. [65], the VBM positions of CIS, CGS, and ZnSnP_2 with respect to the vacuum level are within 0.1 eV. The position of doubly occupied DX single-particle level is 0.7 eV from the VBM in ZnSnP_2 , and Lany and Zunger [21] (Pohl and Albe [19]) have reported that those of In_{Cu} in CIS and Ga_{Cu} in CGS are 0.6 (0.6) and 0.5 (0.55) eV; thus they are well aligned relative to the vacuum level although the constituent elements are different. On the other hand, the thermodynamical transition level in ZnSnP_2 (1.5 eV from the VBM) is slightly higher than that in CGS (0.9 [21] or 1.3 eV [19]).

4. Dominant defects and carrier concentrations

Figures 10(a) and 10(b) summarize the defect formation energies at vertices A (a Zn- and Sn-rich condition) and C (a Zn- and Sn-poor condition) in Fig. 2 as a function of the Fermi level. Once the defect formation energies are obtained, we can calculate defect concentrations. Supposing that the entropy

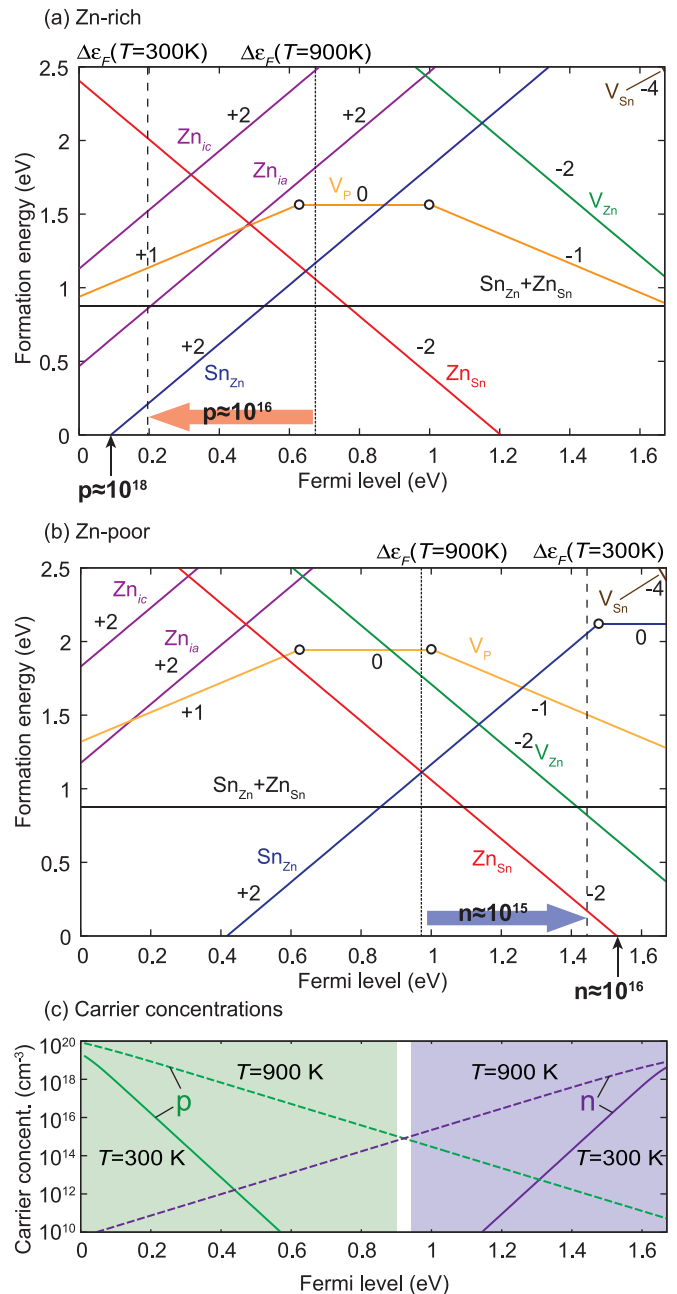


FIG. 10. (Color online) Defect formation energies at (a) A (the Zn- and Sn-rich condition) and (b) C (the Zn- and Sn-poor condition) in the chemical potential diagram shown in Fig. 2. The defects not specified here have higher energies than 2.5 eV at any Fermi level. The formation energy of a pair of antisite defects $\text{Sn}_{\text{Zn}} + \text{Zn}_{\text{Sn}}$ is also shown. The equilibrium Fermi levels without doping at 900 K and those quenched to 300 K are calculated (see text in detail). The carrier concentrations at the quenched Fermi levels and the upper limits due to the Fermi level pinning are also depicted in the unit of cm^{-3} . (c) Equilibrium carrier concentrations as a function of the Fermi level at 300 and 900 K.

and pressure contributions to the Gibbs free energy of defect formation are negligibly small, the defect concentration (*C*) is

TABLE III. Defect and carrier concentrations at chemical potential conditions A and C in Fig. 2 in the unit of cm^{-3} . Temperature is set at 900 K.

Condition	$\text{Zn}_{\text{Sn}}^{-2}$	Sn_{Zn}^2	V_{P}^{-1}	V_{P}^0	V_{P}^1	V_{Zn}^{-2}	$(\text{Sn}_{\text{Zn}} + \text{Zn}_{\text{Sn}})^0$	p	n
A	10^{16}	10^{15}	10^{12}	10^{14}	10^{13}	10^5	10^{18}	10^{16}	10^{13}
C	10^{16}	10^{16}	10^{11}	10^{12}	10^9	10^{12}	10^{18}	10^{14}	10^{15}

calculated through a Boltzmann distribution as

$$C[D^q] = N[D] \exp\left(-\frac{E_f[D^q]}{k_B T}\right), \quad (7)$$

where $N[D]$ is the number of sites for defect D times its spin degeneracy, k_B is the Boltzmann's constant, and T is the absolute temperature. The electron concentration in the conduction band (n) and hole concentration in the valence band (p) are obtained from the Fermi-Dirac distribution as

$$n = \int_{\epsilon_{\text{CBM}}}^{\infty} D(\epsilon) \frac{1}{e^{(\epsilon - \epsilon_F)/k_B T} + 1} d\epsilon, \quad (8)$$

$$p = \int_{-\infty}^{\epsilon_{\text{VBM}}} D(\epsilon) \frac{1}{e^{(\epsilon_F - \epsilon)/k_B T} + 1} d\epsilon, \quad (9)$$

where $D(\epsilon)$ is the density of states in bulk. Figure 10(c) shows the calculated carrier concentrations at 300 and 900 K as a function of the Fermi level in ZnSnP_2 . The defect and carrier concentrations are constrained by the condition of the charge neutrality,

$$p - n + \sum q C[D^q] = 0. \quad (10)$$

By numerically solving this equation self-consistently, we can determine the defect and carrier concentrations, and the Fermi level [66].

The calculated Fermi level and defect and carrier concentrations at 900 K are shown in Figs. 10(a), 10(b), and Table III. In addition, we calculated the Fermi levels at 300 K on the premise that defect concentrations are quenched from 900 K, but the defects can take different charge states in the ratio determined by the Boltzmann distribution. After quenching, the Fermi levels at 300 K are significantly close to the VBM (p type) or CBM (n type) compared with those at 900 K. Sustaining the net carrier concentration generated at 900 K requires the Fermi level to approach the band edges at 300 K. As seen in Fig. 10, both p - and n -type ZnSnP_2 can be attained by changing the growth condition. Under the Zn-rich condition, ZnSnP_2 is p type, while it becomes n type under the Zn-poor condition although carrier concentrations are not very high ($\approx 10^{15} \text{cm}^{-3}$).

It is noteworthy that Sn_{Zn} and Zn_{Sn} have lower formation energies than V_{Zn} and Zn_i , and thus primarily determine carrier type and concentrations. This is different from the experimental suggestion that Zn vacancies would be the main source of holes [11,12], and in contrast with the defects in CIS and CGS, in which V_{Cu} , Cu_i , and antisites can have low

formation energies below 1 eV depending on the Fermi level and chemical potentials [19]. Extrinsic doping is desirable for attaining n -type doping of ZnSnP_2 , but the antisites lead to Fermi level pinning and hinder both electron and hole carrier injections with significantly high concentrations ($p \leq 10^{18}$ and $n \leq 10^{16}$). The formation of Sn_{Zn} DX center does not alter the carrier concentration since the thermodynamical transition level is higher than the pinning level of the Zn_{Sn} acceptor even under the Zn-poor condition.

We also calculated the antisite defect complex in the neutral charge state $(\text{Sn}_{\text{Zn}} + \text{Zn}_{\text{Sn}})^0$, which would be the most abundant complex in ZnSnP_2 . The initial structure was constructed by swapping Zn and Sn neighboring each other. As shown in Figs. 10(a) and 10(b), its formation energy is significantly low and independent of the growth condition, and the binding energy of $\text{Sn}_{\text{Zn}}^{+2}$ and $\text{Zn}_{\text{Sn}}^{-2}$ is -1.35 eV/pair. Such a neutral complex does not affect the carrier concentration, but when Sn_{Zn} becomes the DX center, a complex of $\text{DX} + \text{Zn}_{\text{Sn}}$ can take the -2 charge state. However, we found that $(\text{DX} + \text{Zn}_{\text{Sn}})^{-2}$ is 0.54 eV higher in energy than $(\text{Sn}_{\text{Zn}} + \text{Zn}_{\text{Sn}})^0$ even in the case where the Fermi level is at the CBM and therefore unstable.

IV. CONCLUSIONS

We systematically investigated the native point defects in ZnSnP_2 using the HSE06 hybrid functional in conjunction with finite-size corrections on defect formation energies and defect single-particle levels. Defects dominating the carrier type and concentrations are suggested to be antisite defects, i.e., Zn_{Sn} (acceptor) and Sn_{Zn} (donor). Although these defects lead to the Fermi level pinning, the pinning levels are not so deep and external doping would allow us to grow p - and n -type ZnSnP_2 . We found that the change of the growth condition might also change the doping type: Zn-rich conditions can lead to p type, while Zn-poor conditions n type. V_{P} has a low formation energy as well as the antisites, but it has only deep donor and acceptor levels. In addition, Sn_{Zn} can be a DX center when the Fermi level is located close to the CBM.

ACKNOWLEDGMENTS

This work was supported by the MEXT Elements Strategy Initiative to Form Core Research Center, Grants-in-Aid for Challenging Exploratory Research (Grant No. 26630316) and Scientific Research on Innovative Areas (Grant No. 25106005) from JSPS, Japan. Computing resources of ACCMS at Kyoto University were used in this work. Visualization of the chemical potential diagram and the isosurface of the wave function square were performed with CHESTA [67] and VESTA [68], respectively.

- [1] J. L. Shay and J. H. Wernich, *Ternary Chalcopyrite Semiconductors: Growth, Electronic Properties, and Applications*, 1st ed. (Pergamon, New York, 1975).
- [2] Y. Yan, C.-S. Jiang, R. Noufi, S.-H. Wei, H. R. Moutinho, and M. M. Al-Jassim, *Phys. Rev. Lett.* **99**, 235504 (2007).
- [3] S. B. Zhang, S.-H. Wei, and A. Zunger, *Phys. Rev. Lett.* **78**, 4059 (1997).
- [4] P. Jackson, D. Hariskos, E. Lotter, S. Paetel, R. Wuerz, R. Menner, W. Wischmann, and M. Powalla, *Prog. Photovolt: Res. Appl.* **19**, 894 (2011).
- [5] P. St-Jean, G. A. Seryogin, and S. Francoeur, *Appl. Phys. Lett.* **96**, 231913 (2010).
- [6] W. Shockley and H. J. Queisser, *J. Appl. Phys.* **32**, 510 (1961).
- [7] T. Yokoyama, F. Oba, A. Seko, H. Hayashi, Y. Nose, and I. Tanaka, *Appl. Phys. Express* **6**, 061201 (2013).
- [8] G. A. Seryogin, S. A. Nikishin, H. Temkin, A. M. Mintairov, J. L. Merz, and M. Holtz, *Appl. Phys. Lett.* **74**, 2128 (1999).
- [9] D. O. Scanlon and A. Walsh, *Appl. Phys. Lett.* **100**, 251911 (2012).
- [10] J. L. Shay, E. Buehler, and J. H. Wernick, *Phys. Rev. B* **2**, 4104 (1970).
- [11] M. Rubenstein and R. W. Ure, Jr., *J. Phys. Chem. Solids* **29**, 551 (1968).
- [12] K. Miyauchi, T. Minemura, K. Nakatani, H. Nakanishi, M. Sugiyama, and S. Shirakata, *Phys. Status Solidi C* **6**, 1116 (2009).
- [13] C. Persson, Y.-J. Zhao, S. Lany, and A. Zunger, *Phys. Rev. B* **72**, 035211 (2005).
- [14] S. Demers and A. van de Walle, *Phys. Rev. B* **85**, 195208 (2012).
- [15] S. B. Zhang, S.-H. Wei, A. Zunger, and H. Katayama-Yoshida, *Phys. Rev. B* **57**, 9642 (1998).
- [16] S. Lany and A. Zunger, *Phys. Rev. Lett.* **93**, 156404 (2004).
- [17] S. Lany and A. Zunger, *Phys. Rev. B* **72**, 035215 (2005).
- [18] J. Pohl, A. Klein, and K. Albe, *Phys. Rev. B* **84**, 121201 (2011).
- [19] J. Pohl and K. Albe, *Phys. Rev. B* **87**, 245203 (2013).
- [20] J. Pohl and K. Albe, *J. Appl. Phys.* **108**, 023509 (2010).
- [21] S. Lany and A. Zunger, *Phys. Rev. Lett.* **100**, 016401 (2008).
- [22] A. A. Vaipolin, N. A. Goryunova, L. I. Kleshchinskii, G. V. Loshakova, and E. O. Osmanov, *Phys. Status Solidi* **29**, 435 (1968).
- [23] P. E. Blöchl, *Phys. Rev. B* **50**, 17953 (1994).
- [24] G. Kresse and J. Furthmüller, *Phys. Rev. B* **54**, 11169 (1996).
- [25] G. Kresse and D. Joubert, *Phys. Rev. B* **59**, 1758 (1999).
- [26] J. Heyd, G. E. Scuseria, and M. Ernzerhof, *J. Chem. Phys.* **118**, 8207 (2003).
- [27] J. Heyd, G. E. Scuseria, and M. Ernzerhof, *J. Chem. Phys.* **124**, 219906 (2006).
- [28] A. V. Krukau, O. A. Vydrov, A. F. Izmaylov, and G. E. Scuseria, *J. Chem. Phys.* **125**, 224106 (2006).
- [29] J. Paier, M. Marsman, K. Hummer, G. Kresse, I. C. Gerber, and J. G. Ángyán, *J. Chem. Phys.* **124**, 154709 (2006).
- [30] H. Akamatsu, Y. Kumagai, F. Oba, K. Fujita, K. Tanaka, and I. Tanaka, *Adv. Funct. Mater.* **23**, 1864 (2013).
- [31] Y. Kumagai, Y. Soda, F. Oba, A. Seko, and I. Tanaka, *Phys. Rev. B* **85**, 033203 (2012).
- [32] R. Ishikawa, N. Shibata, F. Oba, T. Taniguchi, S. D. Findlay, I. Tanaka, and Y. Ikuhara, *Phys. Rev. Lett.* **110**, 065504 (2013).
- [33] M. Choi, F. Oba, Y. Kumagai, and I. Tanaka, *Adv. Mater.* **25**, 86 (2013).
- [34] J. P. Perdew, K. Burke, and M. Ernzerhof, *Phys. Rev. Lett.* **77**, 3865 (1996).
- [35] S. B. Zhang and J. E. Northrup, *Phys. Rev. Lett.* **67**, 2339 (1991).
- [36] C. Freysoldt, B. Grabowski, T. Hickel, J. Neugebauer, G. Kresse, A. Janotti, and C. G. Van de Walle, *Rev. Mod. Phys.* **86**, 253 (2014).
- [37] Y. Kumagai and F. Oba, *Phys. Rev. B* **89**, 195205 (2014).
- [38] J. P. Perdew and A. Zunger, *Phys. Rev. B* **23**, 5048 (1981).
- [39] S. L. Dudarev, G. A. Botton, S. Y. Savrasov, C. J. Humphreys, and A. P. Sutton, *Phys. Rev. B* **57**, 1505 (1998).
- [40] M. Cococcioni and S. de Gironcoli, *Phys. Rev. B* **71**, 035105 (2005).
- [41] Y. Kumagai, F. Oba, I. Yamada, M. Azuma, and I. Tanaka, *Phys. Rev. B* **80**, 085120 (2009).
- [42] Y. Kumagai, A. Seko, F. Oba, and I. Tanaka, *Phys. Rev. B* **85**, 012401 (2012).
- [43] J. Tao, J. P. Perdew, V. N. Staroverov, and G. E. Scuseria, *Phys. Rev. Lett.* **91**, 146401 (2003).
- [44] J. Sun, M. Marsman, G. I. Csonka, A. Ruzsinszky, P. Hao, Y.-S. Kim, G. Kresse, and J. P. Perdew, *Phys. Rev. B* **84**, 035117 (2011).
- [45] Y. Hinuma, F. Oba, Y. Kumagai, and I. Tanaka, *Phys. Rev. B* **86**, 245433 (2012).
- [46] Y. Hinuma, F. Oba, Y. Kumagai, and I. Tanaka, *Phys. Rev. B* **88**, 035305 (2013).
- [47] F. Tran and P. Blaha, *Phys. Rev. Lett.* **102**, 226401 (2009).
- [48] P. E. Blöchl, O. Jepsen, and O. K. Andersen, *Phys. Rev. B* **49**, 16223 (1994).
- [49] C. Kittel, *Introduction to Solid State Physics*, 8th ed. (John Wiley and Sons, New York, 2005).
- [50] C. Freysoldt, J. Neugebauer, and C. G. Van de Walle, *Phys. Rev. Lett.* **102**, 016402 (2009).
- [51] C. Freysoldt, J. Neugebauer, and C. G. Van de Walle, *Phys. Status Solidi B* **248**, 1067 (2011).
- [52] H.-P. Komsa, T. T. Rantala, and A. Pasquarello, *Phys. Rev. B* **86**, 045112 (2012).
- [53] W. Chen and A. Pasquarello, *Phys. Rev. B* **86**, 035134 (2012).
- [54] S. Baroni and R. Resta, *Phys. Rev. B* **33**, 7017 (1986).
- [55] M. Gajdoš, K. Hummer, G. Kresse, J. Furthmüller, and F. Bechstedt, *Phys. Rev. B* **73**, 045112 (2006).
- [56] C. G. Van de Walle and J. Neugebauer, *J. Appl. Phys.* **95**, 3851 (2004).
- [57] G. Makov and M. C. Payne, *Phys. Rev. B* **51**, 4014 (1995).
- [58] F. Oba, A. Togo, I. Tanaka, J. Paier, and G. Kresse, *Phys. Rev. B* **77**, 245202 (2008).
- [59] C. W. M. Castleton, A. Höglund, and S. Mirbt, *Phys. Rev. B* **73**, 035215 (2006).
- [60] G. Zhang, A. Canning, N. Grønbech-Jensen, S. Derenzo, and L.-W. Wang, *Phys. Rev. Lett.* **110**, 166404 (2013).
- [61] M. Jain, J. R. Chelikowsky, and S. G. Louie, *Phys. Rev. Lett.* **107**, 216803 (2011).
- [62] S. Lany and A. Zunger, *Phys. Rev. B* **81**, 113201 (2010).
- [63] W. Chen and A. Pasquarello, *Phys. Rev. B* **88**, 115104 (2013).
- [64] P. A. Schultz, *Phys. Rev. Lett.* **96**, 246401 (2006).
- [65] Y. Hinuma, F. Oba, Y. Nose, and I. Tanaka, *J. Appl. Phys.* **114**, 043718 (2013).
- [66] C. Kittel, *Thermal Physics*, 2nd ed. (W. H. Freeman, London, 1980).
- [67] N. Hatada, <http://www.aqua.mtl.kyoto-u.ac.jp/chesta.html>.
- [68] K. Momma and F. Izumi, *J. Appl. Crystallogr.* **41**, 653 (2008).